Experiments in Fluids 21 (1996) 57–65 © Springer-Verlag 1996

The investigation on the properties and structures of starting vortex flow past a backward-facing step by WBIV technique

G. X. Shen, G. Y. Ma

Abstract An experimental investigation of a starting vortex flow around a backward-facing step was conducted in a water channel. The properties and structures of the flow were investigated by qualitative flow visualization using the hydrogen bubble method and by quantitative velocity and vorticity measurements using White-light Bubble Image Velocimetry (WBIV) – a newly developed PIV method. Some invariant properties and 4-stage structures of starting vortex flow were observed.

List of symbols

a	flow acceleration during starting stage
h	height of backward-facing step
$\bar{d}_v$	dimensionless vortex size
t	time
$\bar{t}$	dimensionless time
U_∞	free uniform velocity
u, v	streamwise and spanwise velocity components respectively
Re	Reynolds number based on a and h
x, y	streamwise and spanwise coordinates respectively in flow field
$\bar{x}_c, \bar{y}_c$	dimensionless vortex center position
ω	vorticity
$\bar{\omega}$	dimensionless vorticity
ω_{max}	maximum vorticity
$\bar{\omega}_{max}$	dimensionless maximum vorticity
Γ	circulation
$\bar{\Gamma}$	dimensionless circulation
ν	kinematic viscosity

1 Introduction

The starting flow around a bluff body is a fundamental and complex flow. This type of flow is widespread in industrial application. Some examples include the dynamic lift of a moving and oscillating wing and the load on a tall building in a strong gust of wind. In comparison with steady flow past a bluff body, there are very important features in addition, such as the size and circulation of the starting vortex which is far larger than those of the steady vortices. Also the structure of the starting vortex is quite different from the vortices shed later. Since the starting vortex flow is an unsteady and non-periodic flow phenomena, it is not easy to investigate quantitatively. Hence most investigations of starting vortex flows were only carried out by flow visualization methods, and only a few quantitative investigations have been done. The results of these measurements have provided geometric parameters of a starting vortex. Some examples include the study of a starting flow over spoilers and double steps by Finaish (1986) and a starting flow around a flat plate by Lian (1989). Recently, the instantaneous velocity measurement of a separated flow behind a rearward facing step using PIV technique was studied by Grant et al. (1992). In that study, the flow field was limited to a mean velocity profile of the separated flow, there was no velocity distribution measurement within the structure of shedding vortex. Also the velocity field measurement of an unsteady separated flow over an impulsively started circular cylinder was investigated using PIV technique by Shih (1993). Detailed instantaneous velocity and vorticity field measurements are used to observe the emergence of local boundary layer interaction and how it initiates the global flow separation.

Until now, it seems that no measurement results of velocity or vorticity distributions for a starting vortex flow have been presented. In this paper, we describe some of our work on a starting flow around a backward-facing step using a newly developed PIV technique – White-light Bubble Image Velocimetry (WBIV). This technique measures instantaneous 2-D velocity field (Shen and Ma 1993). It is suitable for the measurement of low speed water flow without the use of expensive, high-power lasers utilized in most PIV experiments.

2 Experimental arrangement and techniques

2.1 Experimental arrangement

The sketch of experimental arrangement to measure velocity distribution of starting vortex flow around 2-D backward-facing step using WBIV technique is shown in Fig. 1. The investigation was conducted in a water channel which was horizontal circulate-type and made of plexiglass. The size of test-cross section was 300×300 mm^2. The flow velocity could be changed by controlling the voltage of the motor. The maximum velocity and acceleration were 100 mm/s and 60 mm/s^2, respectively. The experimental model was a 2-D

Received: 23 April 1993/Accepted: 13 November 1995

G. X. Shen, G. Y. Ma
Fluid Mechanics Institute, Beijing University of Aeronautics and Astronautics, Beijing 100083, China

Correspondence to: G. X. Shen

This work was supported by the CNSF Grant 1939 100-1-3

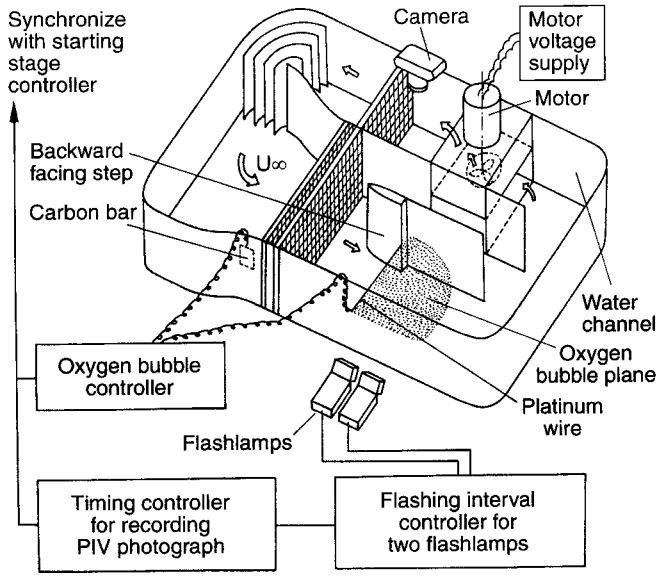

Fig. 1. The sketch of experimental arrangement to measure velocity distribution of starting vortex flow around backward-facing step using WBIV technique

backward-facing step. The height of the step was 20 mm. The front section of this test model was a structure with 2D-C_4 wing profile for uniform flow distribution.

2.2 PIV photograph recording

The principal schematic of WBIV technique can also be found in Fig. 1. WBIV is a form of PIV.

Oxygen bubble: In Fig. 1, oxygen bubbles, instead of solid particles, were used as PIV particles. Because the bubble is soluble in water, it thus forms a good marker in the water channel without dusty pollution. As known to all, when water electrolyzes, oxygen bubbles and hydrogen bubbles, which generate at positive and negative electrodes separately, are swept off by hydrodynamic force and follow the fluid flow. A very fine metal wire, usually 10–50 μm in diameter, may be employed as one of two electrodes of a DC circuit in water channel. Other electrode can be any convenient part of the channel or an inserted metal electrode. By proper control of working conditions, very fine oxygen bubbles will generate from the wire.

In Fig. 1, a platinum wire, 25 μm in diameter, was used as the positive electrode. It was straightened between the sharp edge of the step and the side-wall of the water channel, parallel with the free water surface. A carbon rod was selected as a negative electrode. A specific oxygen bubble controller supplied continuous or pulsed voltages for two electrodes. With continuous work voltage, a sheet-like oxygen bubble plane generated naturally from the straight wire for the starting vortex flow around 2-D backward-facing step (2-D flow field).

The size of oxygen bubbles is of the order of the diameter of electrolyzing wire. Besides wire diameter, the bubble size can also be affected by the work current through the wire. In our experiment, the diameters of the oxygen bubbles were about 20 μm. The bubbles were small enough for flow motion response.

The number density of oxygen bubbles was about 60 bubbles/mm^2. High particle number density is advantageous to increase signal-to-noise ratio of PIV photograph. According to our computer simulation results (Ma and Shen 1994), the number of particle image pairs within interrogation spot of the PIV photograph should be at least 5. The number density of hydrogen bubbles is much higher than that of oxygen bubbles. Unfortunately, hydrogen bubbles are not suitable for the PIV method to record double or multiple exposure images on one film. The number density of hydrogen bubbles is too high to obtain separated bubble real images on the film using white light source. Also it is not high enough to produce speckle pattern using laser source. So either Young's fringes or auto-correlation methods will fail to interrogate the photograph with double or multiple exposures. If using hydrogen bubbles as tracer, the flow field image may be recorded by CCD camera. One frame contains only single exposure images of flow field. Although the images of hydrogen bubbles will overlap each other on each frame, the velocity distribution may be interrogated by using intensity cross-correlation method based on the similarity of intensity distribution between two sequential pictures.

White light source: A white light flashlamp set, instead of general high power pulsed lasers, was used as recording light source for double exposures. The time interval T between two flashlamps was controlled by a flashing interval controller. Controlling time interval was between 1 and 999 ms. For different accelerations ($a = 1.45$, 2.98, 4.48 cm/s^2), the time interval between two flashlamps was selected between 10–20 ms according to testing conditions. The pulsed width τ of flashlamps was 1 ms. Since the bubbles were already a sheet-like plane, it was unnecessary to optically form a light sheet to illuminate the fluid. The light of the flashlamps was directly used to illuminated the oxygen bubble plane.

Recording: The camera was positioned perpendicular to the bubble plane. The angle between the incident axes of the flashlamps and the optical axis of the camera was adjusted to be about 120° to obtain strong scattering light from the bubble plane. The bubble images with double exposures were recorded in white-black film (25 × 35 mm^2, ISO64 Fuji). The recording megnification was 0.33.

As shown in Fig. 2, so long as the positions of the bubbles were not too far from the focus plane (X–Y section), whether the bubbles were in the plane or out of the plane during the time interval of the two exposures, all their images were recorded in the film as only the in-plane components of the bubbles displacements.

Timing controller: A specific timing controller was used to provide different time delay T_s between two instants of the beginning of starting stage and recording of PIV photograph. By changing the delay time T_s of the timing controller, starting the flow and recording the double exposures of flow fluid repeatedly, a set of PIV photographs, which correspond to different instants during starting stage of flow, could be obtained.

A set of typical PIV photographs obtained using WBIV technique is shown in Fig. 3.

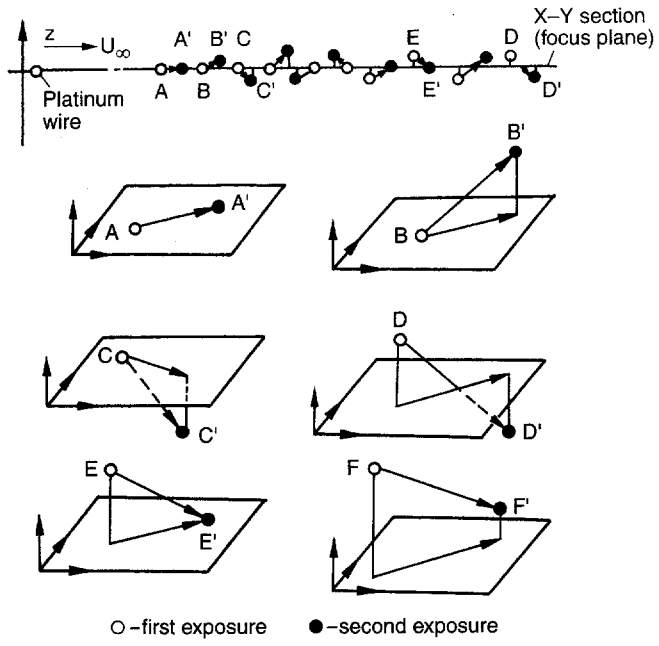

Fig. 2. The in-focus plane components of the bubbles displacements

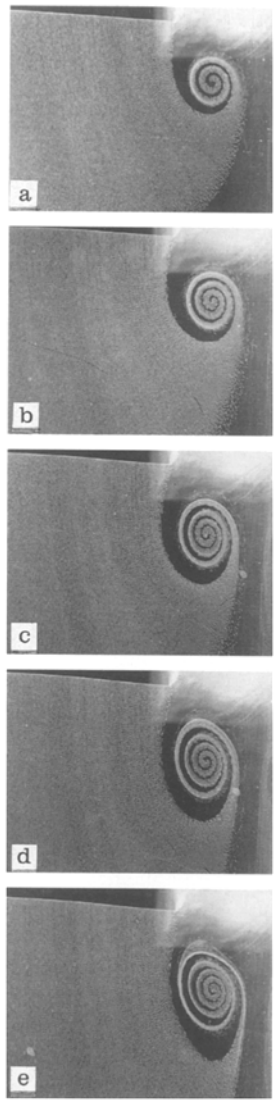

Fig. 3a–e. A set of typical PIV photographs obtained using WBIV technique ($a = 2.98$ cm/s^2)

2.3
PIV photograph interrogation

The PIV photographs were interrogated using Young's fringe method. The auto-interrogation system for PIV photographs using Young's fringe method was set in BUAA (Ma and Shen 1992). The resolution of the digital Young's fringe image was 512 × 512 pixels. The diameter of interrogation laser beam was 0.8 mm. Different sizes of interrogation meshes were used here for every PIV photograph in order to reduce interrogation time. Inside vortex area, the size of interrogation mesh was 0.5 mm × 0.5 mm. Outside vortex area, velocity vectors did not varied very much, then the size of interrogation mesh was 1 mm × 1 mm.

We developed an improved Young's fringe image processing software (Ma and Shen 1992). The fringe orientation is determined by searching the maximum of the orientation function $W(\alpha)$ which is constructed from 2-D Young's fringe intensity distribution by 1-D average-correlation method. The influence of diffraction halo is removed by a simulated function constructed with normal function. The fringe spacing is derived by calculating 1-D Fourier transformation of 1-D compressed Young's fringe intensity distribution along fringe orientation. This method is not sensitive to secondary speckle noise in Young's fringes. A high measurement accuracy can be obtained. The measurement error of fringe orientation and spacing are less than 0.5° and 1% respectively. Furthermore, a smaller of computation is required.

Because of the ambiguity in determining the direction of velocity using Young's fringe method without any image shifting technique, software for determining the direction of velocity was developed, which was based on the knowledge of the direction of the main flow, the approximate positions of the vortex center and the reattached point for starting vortex flow behind the step. First, the PIV photograph is interrogated by Young's fringe method. According to the interrogation result, the approximate positions of vortex center and reattachment point could be determined. Then, the reference directions generated automatically for every interrogation mesh point based on these rough knowledge. As shown in Fig. 4, the real line indicates the orientation and magnitude of local velocity of interrogation mesh point which is obtained using Young's fringe method. The dashed line with arrowheads is the reference direction of velocity. Finally, the directions of velocity are automatically obtained for every interrogation point. The directions of velocity is the one which is at smaller angle with the reference direction. For example, the velocity directions of the point *A*, *B*, *C*, *D*, *E*, *F* are shown in Fig. 4 respectively.

2.4
Advantages and limitations of WBIV

The main advantages for WBIV can be summarized as following. (a) Without dusty pollution to water channel; (b) The

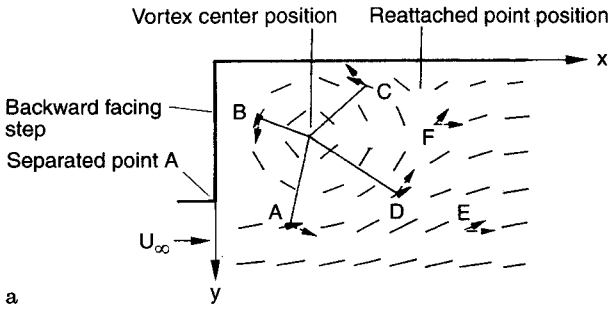

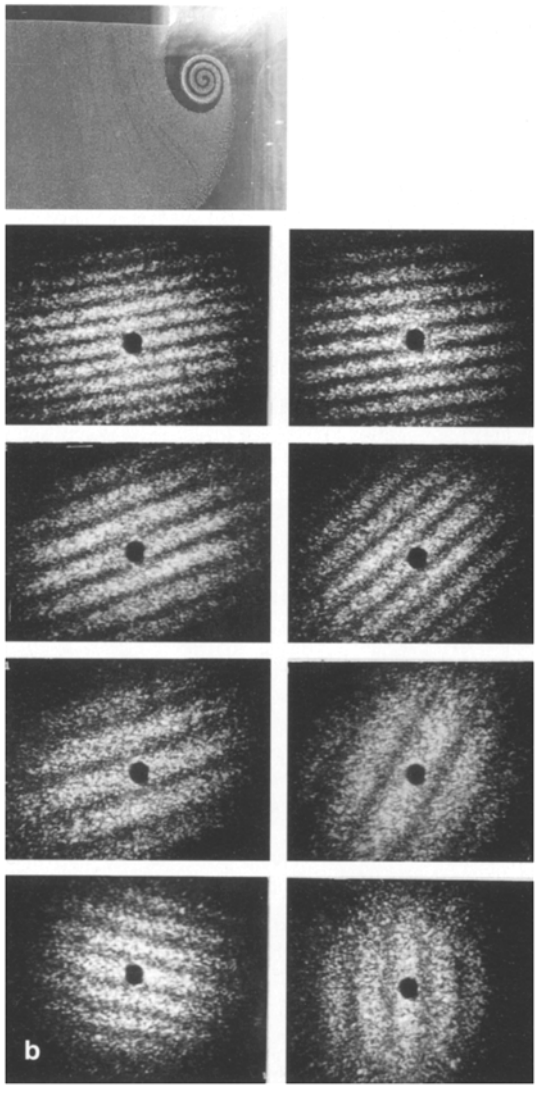

Fig. 4a,b. Schematic of determining velocity direction by software method

experimental cost is much lower than using an expensive, high power laser light source; (c) High-quality PIV phtograph which corresponds to Young's fringes with high signal-to-noise ratio could be obtained. The reasons are as following: Besides uniform shape of bubbles and appropriate high density of bubble number, there are no particles outside the sheet-like bubble plane. Usually solid particles outside the sheet-like bubble plane could produce noisy scattering light or envelop the particle within the sheet-light section; (d)The PIV photograph can be employed either for quantitative velocity measurement or for qualitative flow visualization, as shown in Fig. 3; (e) Because there is only a thin sheet of bubbles in flow field, the transparency of flow field is high and the disturbance caused by bubbles is low compared with solid particles which fill with whole flow field.

Certainly, also there are some limitations for WBIV. (a) It seems only suitable for low speed water flow; (b) One should consider the effects of solution, diffusion and buoyancy of bubbles; (c) It is not suitable for strongly three dimensional flow, in that case the bubble plane would be overlapped and shrunk.

3
Results and discussion

3.1
Non-dimensionalization

In order to correlate the results of various flow acceleration stages and compare with previous results by other researchers, coordinate system (x, y), time t, velocity v, vorticity ω and circulation Γ were non-dimensionalized.

$$\begin{aligned}
\bar{x}&=\frac{x}{x^*}, & x^*&=h\\
\bar{y}&=\frac{y}{y^*}, & y^*&=h\\
\bar{t}&=\frac{t}{t^*}, & t^*&=\sqrt{\frac{2h}{a}}\\
\bar{v}&=\frac{v}{v^*}, & v^*&=\frac{h}{t^*}=\sqrt{\frac{ah}{2}}\\
\bar{\omega}&=\frac{\omega}{\omega^*}, & \omega^*&=\frac{1}{t^*}=\sqrt{\frac{a}{2h}}\\
\bar{\Gamma}&=\frac{\Gamma}{\Gamma^*}, & \Gamma^*&=\omega^* h^2=\sqrt{\frac{ah^3}{2}}
\end{aligned} \tag{1}$$

According to $h=\frac{1}{2}at^{*2}$, the physical meaning of characteristic time t^* and characteristic velocity u^* are the time and the average velocity respectively for a particle passing through distance h (the height of step) with acceleration a from stationary state. The Reynolds number Re is defined as

$$Re=\frac{4u^*h}{v}=\frac{\sqrt{8ah^3}}{v} \tag{2}$$

Here all the definitions of parameters for non-dimensionalization and the Re number are based on the flow acceleration a and step height h.

3.2
Flow visualization

First the starting vortex patterns, as in most previous works, were visualized by hydrogen bubble method for three accelerations: $a=1.45$, 2.98, 4.48 cm/s^2 ($Re=960$, 1380, 1690 respectively). The experimental arrangement was similar to the

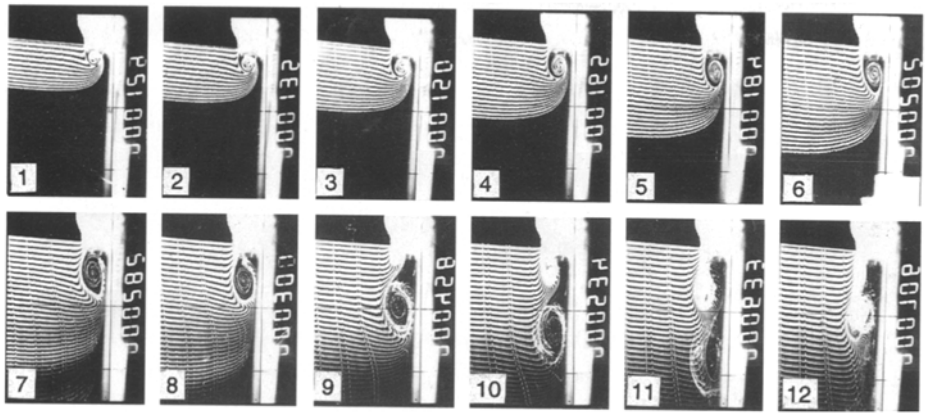

Fig. 5. Flow visualization photographs with time history for starting vortex flow around backward-facing step by Hydrogen bubble method ($a = 1.45$ cm/s^2)

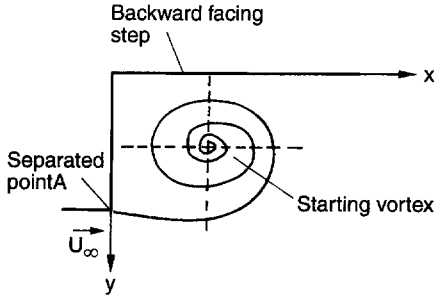

Fig. 6. Coordinate system in flow field

one used in the WBIV technique (Fig. 1). However the platinum wire was used as a cathode and hydrogen bubbles were produced as tracers. A stage lamp with 1000 W power was used as light source. Photographs were consecutively recorded by a movie camera with a recording speed 32 frames/s. A time history of flow visualization photographs is shown in Fig. 5. The total evolution of the starting vortex flow passing the backward-facing step can be observed from those photographs. Later, we will discuss the evolution stages of the vortex flow from the pictures with the velocity and vorticity measurement results using WBIV technique. The coordinate system of flow field is shown in Fig. 6. The dimensionless geometrical vortex center positions with time-history obtained from flow visualization photographs are shown in Fig. 7. An invariant law of vortex center positions for various testing accelerations is shown in Fig. 7. This closely agrees with previous results for different testing models (Finaish 1986; Lian 1989).

3.3
Instantaneous velocity distribution measurement

The evolution of velocity distribution with time for the starting vortex flow with three testing accelerations $a = 1.45$, 2.98, 4.48 cm/s^2 ($Re = 960$, 1380, 1690 respectively) were measured in detail using WBIV technique. Typical results of velocity distributions for $a = 1.45$ cm/s^2 are shown in Fig. 8. The growth of the starting vortex, the secondary induced-vortex and the second separated vortex, reattached point position, can be seen in Fig. 8. The time histories of dimensionless positions of reattachment point for three testing accelerations are shown in Fig. 9.

In Fig. 8, there are some blanks in which there are no measured velocity vectors. In these areas, there is no oxygen bubble distribution or the magnitude of velocity is low there is so that the displacements is too small to be measured.

3.4
Vorticity distribution

From instantaneous velocity measurement results, the vorticity distribution could be obtained according to the following formula,

$$\omega_{i,j} = -\frac{u_{i,j+1} - u_{i,j-1}}{2\delta y} + \frac{v_{i+1,j} - v_{i-1,j}}{2\delta x} \tag{3}$$

where ω_{ij} is the vorticity and u_{ij} and v_{ij} are the velocity components in interogation mesh point P_{ij}. δ_x and δ_y are interrogation mesh intervals in x and y directions respectively. A time history of iso-vorticity contour maps in the starting vortex flow is shown in Fig. 10 for $a = 1.45$ cm/s^2. As shown in Fig. 8, the evolution of starting vortex in several different stages is revealed.

3.4.1
Vortex center position

There has been no rigorous definition about vortex center position. Pulln (1980) considered that the position which corresponded to the maximum of vorticity within vortex distribution region was defined as vortex center. Because of the measurement difficulty for vorticity distribution, the geometrical center position of the starting vortex obtained from flow visualization patterns was usually taken as vortex center position (geometrical vortex center). Here the dimensionless vortex center positions were obtained by locating the position of maximum vorticity (vorticity vortex center) (Fig. 7). As shown in Fig. 7, the geometrical vortex center position is close to the vorticity vortex center position.

3.4.2
Vortex size

From the results, more than 95% of vorticity flux is concentrated within the region bounded by the iso-vorticity contour $\bar{\omega} = 0.5$. This region can be considered as the spatial size of the starting vortex. Based on this vortex size criterion,

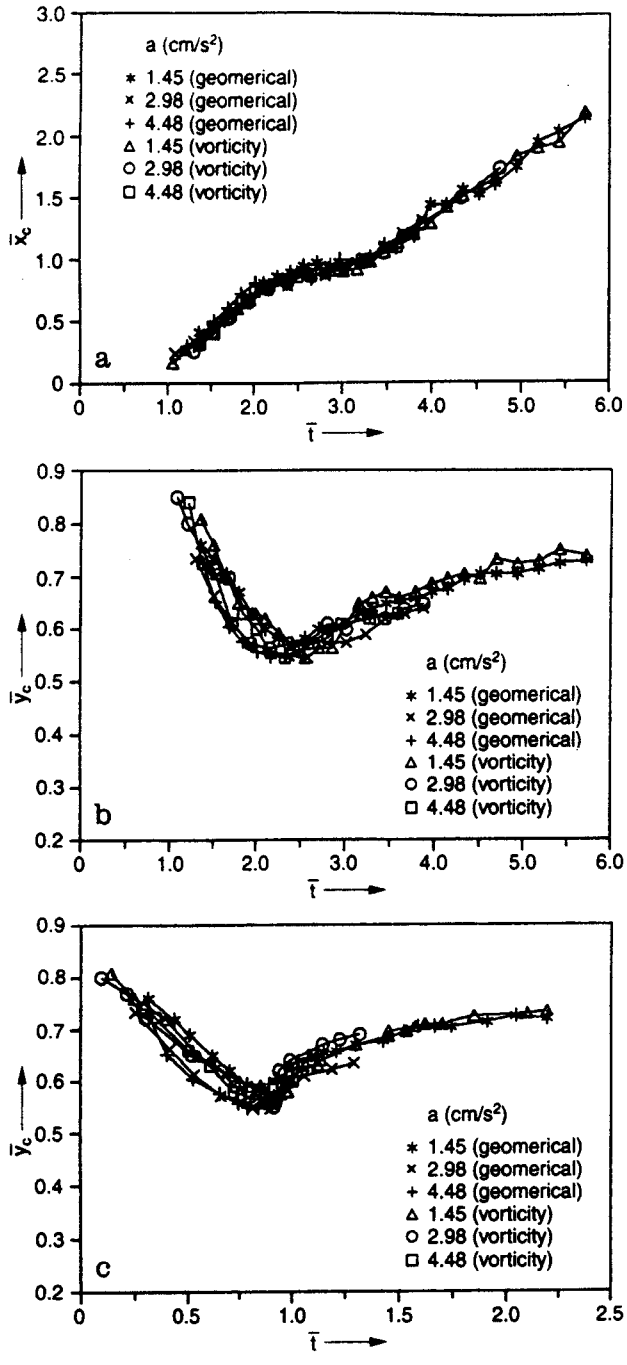

Fig. 7a–c. Dimensionless vortex center positions with time-history for three starting accelerations. a The position along x direction; b the position along y direction; c the trajectory

a time histories of vortex sizes for three testing accelerations are shown in Fig. 11.

3.4.3
Maximum vorticity and circulation

Time histories of dimensionless maximum vorticity and circulation of a starting vortex for three testing accelerations are shown in Figs. 12 and 13 respectively. The maximum vorticity and the circulation were calculated from the following equations respectively,

$$\omega_{\max} = \mathrm{MAX}\ (\omega)|_A \qquad (4)$$

$$\Gamma = \int_A \omega \, d\sigma,$$

where A is the distribution region of the starting vortex within the boundary for iso-vorticity contour $\bar{\omega} = 0.5$, and $d\sigma$ is 2-D integral element.

3.5
Measurement result discussion

The evolution procedure of starting vortex flow around a backward-facing step can be described as occurring in four stages, as shown in Fig. 14.

(1) First acceleration stage

During this stage, as shown in Figs. 14a and 5(1–3), the flow accelerates from a stationary state with constant acceleration. Since vorticity accumulates from shear layer continuously, both the maximum vorticity and the circulation increase with time approximately linearly ($d(\omega_{\max})/d\bar{t} \approx 11.7$, Fig. 12, $d(\bar{\Gamma})/d\bar{t} \approx 2.47$, Fig. 13). The size of the starting vortex grows linearly with time ($d(\bar{d}_v)/d\bar{t} \approx 0.48$, in Fig. 11). As shown in Fig. 7, the vortex center position moves downstream slowly ($d(\bar{x}_c)/d\bar{t} \approx 0.47$) and also approaches to the bottom wall gradually ($d(\bar{y}_c)/d\bar{t} \approx 0.15$). The shear layer from separated point A remains thin and laminar. The iso-vorticity contours are smooth and round in shape. The velocity and vorticity distribution maps shown in Fig. 8a and Fig. 10a, respectively, belong to this stage.

2) Second acceleration stage

During this stage, as shown in Figs. 14b and 5(4–6), the flow is still accelerating, but the acceleration slows down and approaches to zero. Due to decreasing acceleration, the vorticity accumulation from the separated point A slows down, although the circulation still keeps growing. The maximum vorticity arrives at a maximum value point and then decreases with time because of the diffusion of vorticity. Another remarkable feature during this stage is that the shear layer becomes thicker while the size of the vortex still keeps growing. The vortex center position moves downstream with almost the same velocity during the first acceleration stage. At the same time, it gradually reaches the minimum distance from the bottom wall ($\bar{y} \approx 0.58$, Fig. 7). The vortex sheet and iso-vorticity contours are still smooth during this stage. The velocity and vorticity distributions shown in Figs. 8b and 10b belong to this stage.

3) Secondary induced vortex and second separated vortex stage

During this stage, as shown in Figs. 14c and 5(7–9), the flow velocity arrives at a constant. Near the bottom wall region, the secondary induced-separated vortex begins to form. With the developing of a secondary induced-separated vortex, the starting vortex sheds from the separated point A and moves downstream. At the same time, the second separated vortex from separated point A begins to form. Since the starting vortex has shed from separated point, it no longer accumulates vorticity. The circulation of the starting vortex decreases. Because of the diffusion of vorticity, the maximum vorticity continues to decrease with time approximately linely

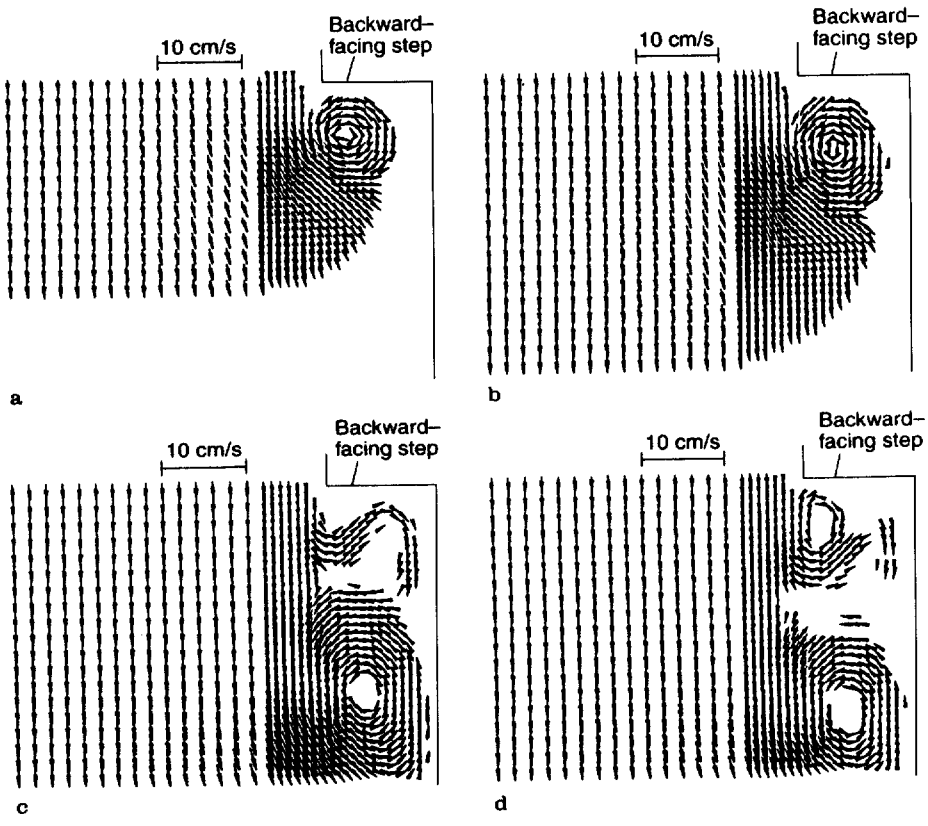

Fig. 8a–d. Typical maps of velocity distribution with time-history for starting vortex flow around backward facing step ($a = 1.45$ cm/s^2). **a** $\bar{t} = 1.66$, ($t = 2.75$ s); **b** $\bar{t} = 1.96$, ($t = 3.25$ s); **c** $\bar{t} = 5.18$, ($t = 8.60$ s); **d** $\bar{t} = 5.72$, ($t = 9.50$ s)

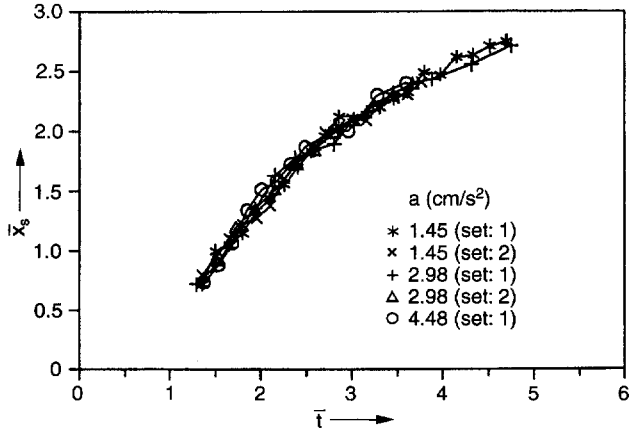

Fig. 9. Dimensionless position of the reattached point with time-history for three texting accelerations

$(d(\omega_{max})/d\bar{t} \approx -1.2$, Fig. 12). During this stage, first the vortex center position moves away from the bottom wall and almost keeps vertically to the bottom wall ($\bar{x} \approx 0.9$, as shown in Fig. 7). Then it moves downstream. Because of the diffusion of vorticity, the vortex size still keeps growing. Because of the instability and the distortion of shear layer, both the vortex sheet and the iso-vorticity contours distort substantially. The velocity and vorticity distributions shown in Figs. 8c and 10c belong to this stage.

4) Breakdown stage

During this stage, as shown in Figs. 14d and 5(10–12), the starting vortex moves downstream with distance $\bar{y} \approx 0.71$ from the bottom wall (Fig. 7). The starting vortex diffuses, distorts further and breaks down into turbulence. At the same time, the second separated vortex keeps developing and sheds from separated point A and then breaks down too. In comparison to the starting vortex, the second separated vortex is much smaller, the shear layer is thicker, the vortex sheet is not as well defined, the vortex strength is much smaller and exists for a much shorter time. The velocity and vorticity distributions shown in Figs. 8d and 10d belong to this stage.

Based on the experimental data of vorticity and circulation for the starting vortex and the second separated vortex, the following quantitative observation can be made

$$\frac{(\omega_{max})_{max_1}}{(\omega_{max})_{max_2}} = 1.6 \sim 2.1 \qquad (5)$$

$$\frac{\Gamma_{max_1}}{\Gamma_{max_2}} = 4.0 \sim 5.3$$

where $(\omega_{max})_{max_1}$ and $(\omega_{max})_{max_2}$ are the maximum value of the maximum vorticity for the starting vortex and the second separated vortex separately, Γ_{max_1} and Γ_{max_2} are the maximum value of the circulation for the two vortices.

Obviously, the starting vortex is much stronger than the following shedding vortices. It shows that the dynamic load for a starting vortex might be 4–5 times larger than the load for the following shedding vorticies during steady flow.

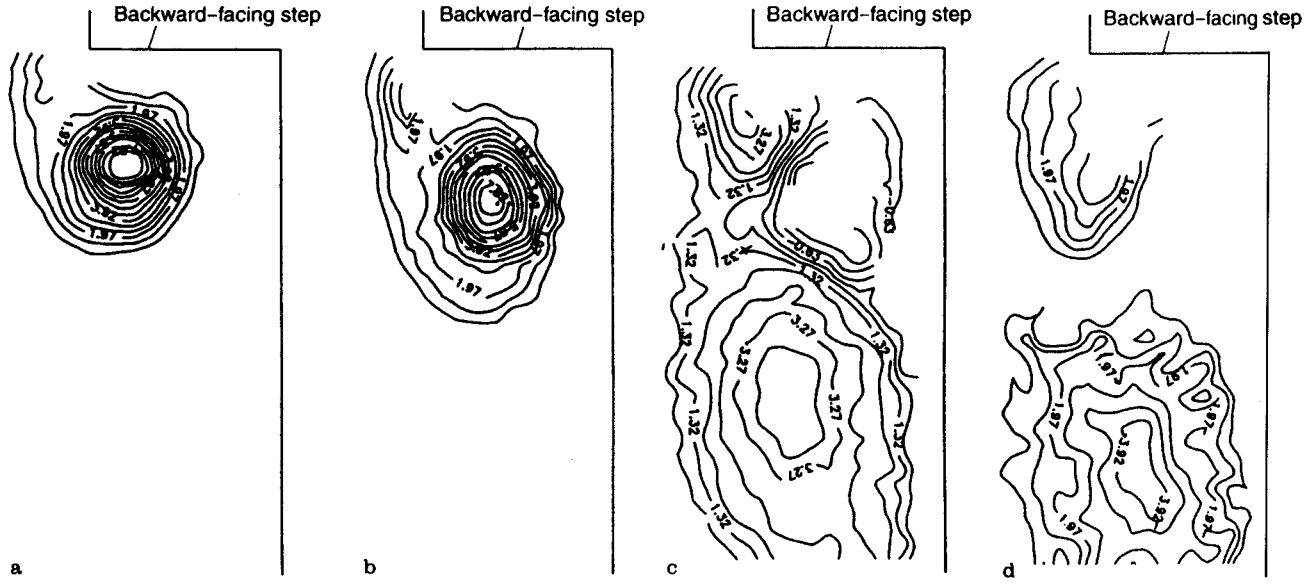

Fig. 10a–d. Typical maps of iso-vorticity contours with time-history for starting vortex flow around backward facing step ($a = 1.45$ cm/s^2). **a** $\bar{t} = 1.81$, ($t = 3.00$ s); **b** $\bar{t} = 2.11$, ($t = 3.50$ s); **c** $\bar{t} = 5.18$, ($t = 8.60$ s); **d** $\bar{t} = 5.72$, ($t = 9.5$ s)

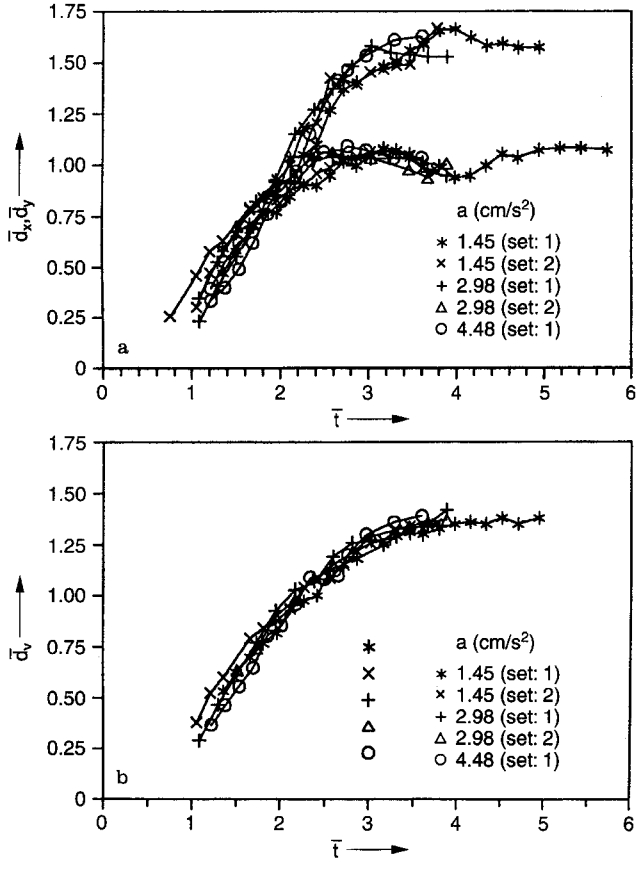

Fig. 11a, b. Dimensionless vortex size with time history for three texting accelerations. **a** Vortex size in x and y direction respectively; **b** Average result of vortex size for x and y direction

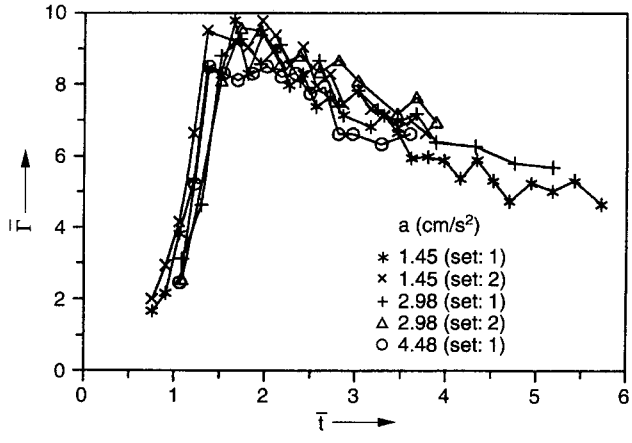

Fig. 12. Dimensionless maximum vorticity with time history for three testing accelerations

4 Conclusion

1) WBIV is a newly developed PIV technique. Instead of solid particles and high power laser used as usual, a sheet of oxygen bubbles is used as tracers without dusty pollution to testing facilities, and a white light flashlamp set is used as light source. Using WBIV technique, a high quality PIV photograph with high signal-to-noise ratio can be obtained. The WBIV techniques is limited to the investigation of 2-D low speed water flow.

2) Using WBIV technique and hydrogen bubble flow visualization technique, the starting vortex flow with three

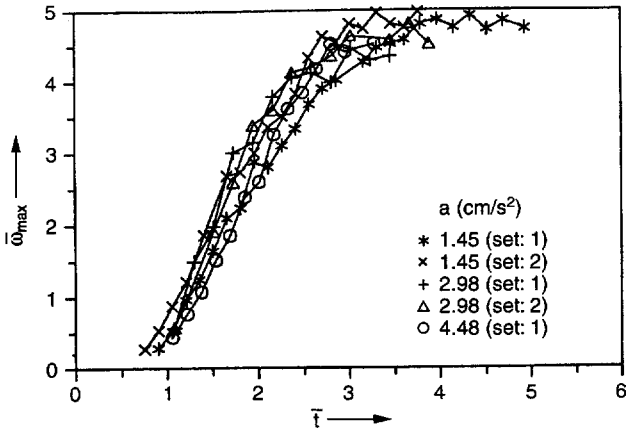

Fig. 13. Dimensionless circulation with time history for three testing accelerations

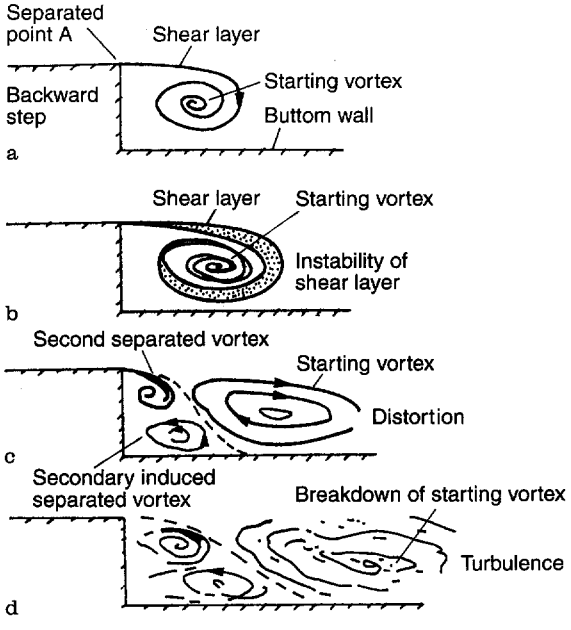

Fig. 14a–d. The schematic of 4-stages of starting vortex flow around backward facing step. **a** stage 1; **b** stage 2; **c** stage 3; **d** stage 4

testing accelerations ($a = 1.45$, 2.98, 4.48 cm/s^2) past a backward-facing step was investigated. The evolution of starting vortex patterns, including the time histories of instantaneous velocity and vorticity distributions were measured. Also the invariant properties of some dimensionless parameters were confirmed in the starting vortex flow.

3) The whole evolution of starting vortex flow could be described as four stages: (1) first acceleration stage, (2) second acceleration stage, (3) secondary induced-separated vortex and second separated vortex stage, (4) breakdown stage.

4) Results presented in this paper show that the starting vortex is much stronger than the following shedding vortex (approximately 4–5 times larger in terms of circulation).

Reference

Adrian RJ (1986) Multi-point optical measurement of simultaneous vectors in unsteady flow-a review. Int J Heat Fluid Flow 7: 127–145

Brucker C; Althaus W (1992) Study of vortex breakdown by PTV. Exp Fluids 13: 339–349

Finaish F; Freymuth P, Bank W (1986) Starting flow over spoiler, double step and cavities. J Fluid Mech 168: 383–392

Grant I; Owens E; Yan YY (1992) Particle image velocimetry measurements of the separated flow behind a rearward facing step. Exp Fluids 12: 238–244

Lian QX (1989) Starting flow and structures of the starting vortices behind bluff bodies with sharp edges. Exp Fluids 8: 95–103

Ma GY; Shen GX (1992) A high accuracy and fast automatic processing method of Young's fringe pattern in PIV. Flow Visualization VI: 895–899

Ma GY; Shen GX (1994a) Analysis of the experimental parameters in PIV. 3nd Asian Symp on Visualization, Japan 723–728

Ma GY; Shen GX (1994b) Description and analysis of intensity distribution of Young's fringes in PIV. Proc. 2nd Intl. Conf. on Fluid Dynamic Meas. and its Applications, Beijing Oct. 221–226

Pulln DI; Perry AE (1980) Some flow visualization experiments on the vortex. J Fluid Mech 97: 239–255

Sethian JA etc. (1988) Validation study of vortex methods. J Comput Phys 74: 283–317

Shen GX; Ma GY (1993) White light bubble image velocimetry. ACTA Aerodyn Sinica 6: 217–223

Shih C etc. (1993) Control of unsteady separation over an impulsive started circular cylinder. AIAA-93-3275